Functionally Graded Alloys from 316 Stainless Steel to Inconel 718 by Powder-Based Laser Direct Energy Deposition

Kun Li, Jianbin Zhan, Peng Jin, Qian Tang, David Z. Zhang, Wei Xiong, and Huajun Cao

Abstract Extreme serving conditions are demanding on materials with functional microstructure and properties. Additive manufacturing (AM) is an efficient method to fabricate complex geometry functionally graded materials (FGMs) with gradually variable composition and structures as a function of position. In this work, a laser-based directed energy deposition (DED) process was carried out to develop a series of compositionally graded joints from 316 stainless steel to Inconel 718 alloy through computational analysis and experimental characterization. The microstructure, composition, and phases were investigated as a function of position in FGMs. Compared to the traditionally fabricated joint, AM graded materials had more gradient composition and microstructure. The computational-experimental approach is a promising method to design good properties of dissimilar metal joints. The gradient zone that can be flexibly tuned by AM process provides a high throughput design through local tailoring of properties to develop new functional materials.

K. Li (✉) · Q. Tang · D. Z. Zhang · H. Cao (✉)
State Key Laboratory of Mechanical Transmission, Chongqing University, Chongqing 400044, China
e-mail: kun.li@cqu.edu.cn

H. Cao
e-mail: hjcao@cqu.edu.cn

K. Li · Q. Tang · D. Z. Zhang
Chongqing Key Laboratory of Metal Additive Manufacturing (3D Printing), Chongqing University, Chongqing 400044, China

K. Li · J. Zhan · P. Jin · Q. Tang
College of Mechanical and Vehicle Engineering, Chongqing University, Chongqing 400044, China

D. Z. Zhang
College of Engineering, Mathematics and Physical Sciences, University of Exeter, North Park Road, Exeter EX4 4QF, UK

W. Xiong
Department of Mechanical Engineering and Materials Science, University of Pittsburgh, Pittsburgh, PA 15261, USA

Introduction

Functionally graded materials (FGMs) possess spatially varying properties with gradual transitions in chemical compositions or structures, which can overcome the defects resulting from the sharp dissimilar joints [1, 2]. The laser-based direct energy deposition (LDED) with the powder feedstock draws the attention on the manufacturing of FGMs because of the flexibility in geometrical structure design, control space, and so on [3–5]. In the present work, we developed successful builds of FGM bulks from 316 stainless steel (SS316) to Inconel 718 superalloy (IN718) by LDED. The element composition, microstructure, and mechanical properties in as-deposited FGMs were evaluated. The aging behaviors on the FGMs were for the first time studied to elucidate the phase transformation and precipitation. The CALPHAD-based (CALculation of PHAse Diagrams) high throughput modeling was performed to predict and compare the phases observed in the experiments, which provides a fundamental guidance for further development on FGMs.

Materials and Experimental Procedure

The IN718 and SS316 powders with a particle size range of 80–125 μm were used for the gradient component building. They were deposited on a substrate plate of 316L stainless steel (SS316L) through two feeders in a directed energy system embedded with a Nd:YAG laser. The building parameters were optimized as a laser power of 300 W, a scan speed of 5 mm/s, a layer thickness of 0.25 mm, and a hatch spacing of 0.50 mm with a scan pattern of 90° between each layer. The printing system is flexible to deposit powders with variable fraction of powders by controlling the feed rates. The FGMs were built from pure SS316 to pure IN718 with an increased weight percent of 25% (25 wt.%). Each composition of the material was applied to deposit four layers.

The deposited blocks were cut into several samples along cross sections parallel to building direction by wire electric discharge machine for metallurgical and mechanical characterization. Some pieces of samples were encapsulated into vacuumed quartz tubes filled with pure argon for post-aging treatments at 718 °C for 15 h, followed by water quenching. All the samples were mounted and polished with standard metallographic methods. The macro-morphology and microstructure as a function of location were observed using OM, SEM, and EBSD.

The phases in this FGM were performed using CALPHAD-based modeling to predict the phases and help microstructural analyses. The TCNI8 database from Thermo-Calc Software [6] was used to compare the calculation of the phase formation

in the FGM. P and S were excluded in the calculation as a simplification. The δ phase was suspended in the calculation of TCNI8 to make sure the presence of γ′ and γ″ phases.

Results and Discussion

FGM Forming Morphologies as a Function of Composition

The overall forming morphologies are revealed in Fig. 1. There were no cracks and big forming distortions in these FGM blocks by our in-house processing control. The representative block was cut along the A-A section, as shown in Fig. 1b. The corresponding OM morphology is presented in Fig. 1c. The melt pools and fusion lines between each laser pass are clear to see after the chemical etching. 20 layers were built up with five compositional gradients, i.e., pure SS316, 25 wt.% IN718,
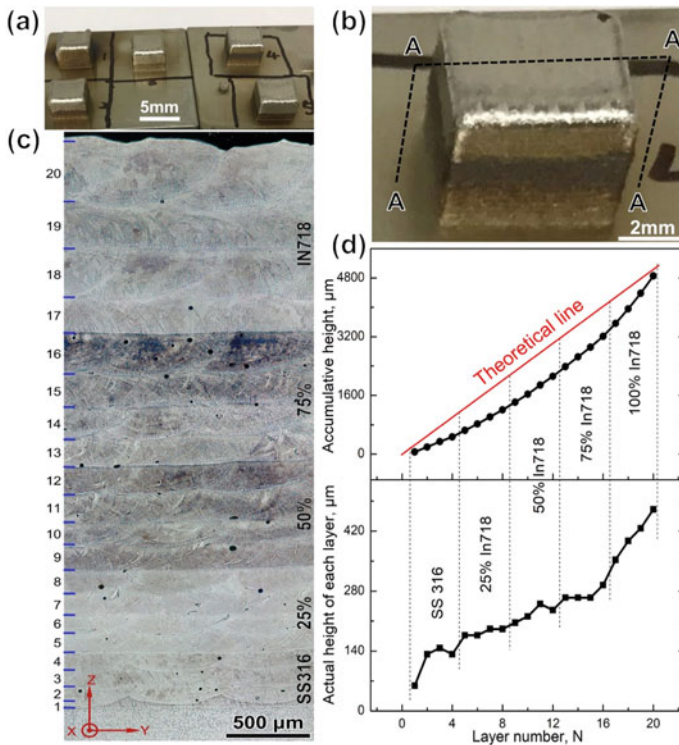

Fig. 1 Overall forming morphologies of as-deposited FGMs **a** final FGM blocks, **b** the investigated FGM block showing cross section A-A of sample slicing, **c** OM morphologies of the FGM along cross section A-A, and **d** layer height distribution

50 wt.% IN718, 75 wt.% IN718, and 100 wt.% IN718. Each compositional gradient has four layers. However, each layer has different actual layer height (H_L), which is increasing gradually as the FGM builds up (Fig. 1d). The accumulative height of layers (H_A) is non-linear and deviated from the theoretical line of the ideal case, because of this mismatch between the actual layer height and the set layer thickness. However, the total built height (H_T) was well controlled at around 5 mm. The increase of H_L can be explained by the changes in the absorption of laser energy and heat accumulation of each layer.

Microstructural Evolution in As-Deposited FGM

The backscatter electron (BSE) morphology and EDS profile of the whole as-deposited FGM along building direction by the multi-step seaming observation are shown in Fig. 2a, b. The EDS analysis was conducted on the finely polished flat surface (Fig. 2a) of the as-deposited FGM without etching. It is obvious that the major elements of Ni and Cr have equal proportional increases, and Fe has an equal proportional decrease from pure SS316 to pure IN718. The alloying element of Nb has a corresponding increase gradually (Fig. 2b). Other alloying elements cannot be quantified accurately due to their low values of contents. However, because the gradient compositions were mixed by two pure powders of SS316 and IN718 with certain weight ratios, all of the elements have the same ratio change in each mixed composition. The major elements of Fe and Ni can represent the real controlling accuracy for the whole gradient compositions. It can be observed that there is a
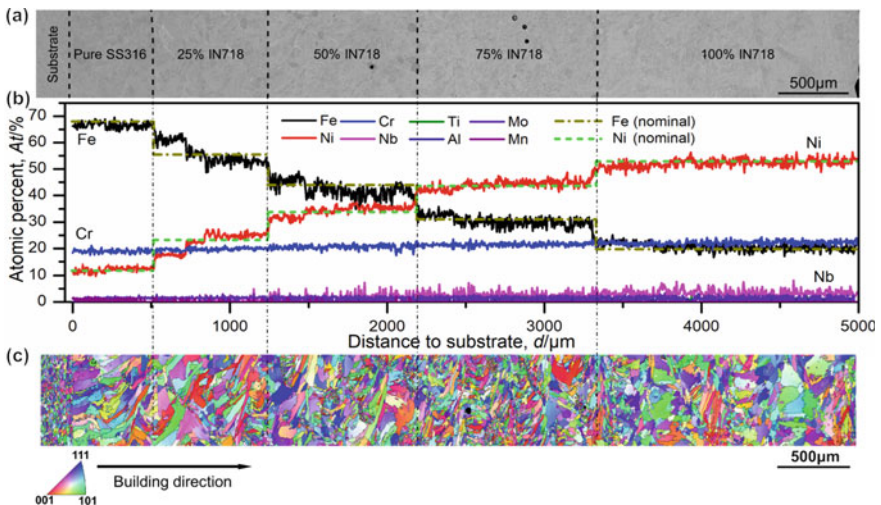

Fig. 2 Electron observation of the as-deposited FGM along building direction **a** BSE morphology, **b** EDS profile, and **c** EBSD profile

flat composition profile in each component that changes from pure SS316 to pure IN718, except few small deviations between each layer like in the compositions of 25 and 5 wt.%. Further comparing the measured composition to the nominal (designed) composition by two representative elements of Fe and Ni, it reveals a well agreement with each other, which demonstrates the successful build of this FGM with a decent control on composition.

The stitched overall EBSD mapping exhibits the grain evolution as the composition changes (Fig. 2c). Only one face center cubic (FCC) γ phase of the matrix exists in the whole FGM, because both SS316 and IN718 have FCC matrix. There are no sharp interfaces between each component with different composition. Each interface has a small gradient zone, especially for those near the higher content of IN718, as demonstrated in EDS profiles of Fe and Ni in Fig. 2b. The gradient zone along each interface lowers the mismatch of printability for two individual compositions, which reduces the possibility of cracks. Another phenomenon worth to notice is that the grains grow from columnar shape to equiaxial form as the weight percent of IN718 increases (Fig. 2b), which is due to the effect of heat capacity on the solidification and grain growth [7–9].

In the as-deposited FGM, it is obvious that the grain orientation shows a strong texture and anisotropy along the building direction. The grain size decreases first and then increases as the weight percent of IN718 increases. The component with 75 wt.% IN718 has the finest grain size (Fig. 2c). The found of this critical composition on the grain size might be explained by the entropy of this component [10, 11], which will be further studied in the next work. This results in the finest grain in the as-deposited component with the composition of 75 wt.% IN718. Moreover, it can be seen that the low angle grain boundary (LAGB) has the highest value at 75 wt.% IN718, which reflects the residual stress and distortion in the grains [12–14]. This 75 wt.% IN718 component with fine and equiaxial grains directly obtained from the laser deposition has a great potential for use in AM industry with the advantage of avoiding post-heat treatments.

Precipitation Behaviors in FGM During Aging

Because of the synergistic effect of gradient compositions and non-equilibrium status from laser deposition, the precipitation behaviors presented in FGMs during aging would have a significant difference from those in the alloys fabricated by the traditional methods. After aged at 718 °C for 15 h, i.e., a peak aging status for IN718 alloy [15, 16], the SEM morphologies of the microstructure in the components with different compositions were observed, respectively, as shown in Fig. 3. It shows that the Laves phase remains in the matrix, even occurring in the matrix of pure SS316 after the long aging time (Fig. 3a). The segregation along columnar dendrites and cellular dendrites becomes serious because of the increased precipitation. Nevertheless, there are new precipitates occurring around the Laves phase, as seen at the high magnification (Fig. 3a3–e3).
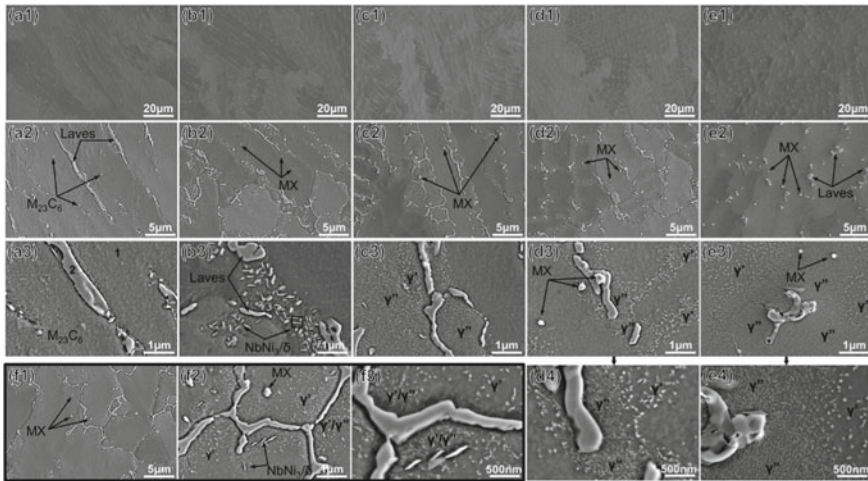
Fig. 3 SEM morphologies of the microstructure in different compositional components of the aged FGM at 718 °C for 15 h **a** Pure SS316, **b** 25 wt.% IN718, **c** 50 wt.% IN718, **d** 75 wt.% IN718, **e** 100 wt.% IN718, and **f** the interface zone between (**b**) and (**c**). ("1–4" present the images at different magnifications, the observed location is in the center zone of each component)

To clarify the precipitates in the aged FGM, the thermodynamic simulation via the CALPHAD database was performed to predict the phase fraction as a function of temperature for different compositions. Because aging for 15 h is a relative equilibrium status which is different from the as-deposited condition, the equilibrium database was used for this simulation. Figure 4 shows the simulation result from TCNI8 from pure SS316 to pure IN718 components. In the pure SS316 component, there are plenty of irregular phases along the grain boundaries and many circular

Fig. 4 Phase fraction versus composition in the FGM from high throughput thermodynamic modeling by TCNI8
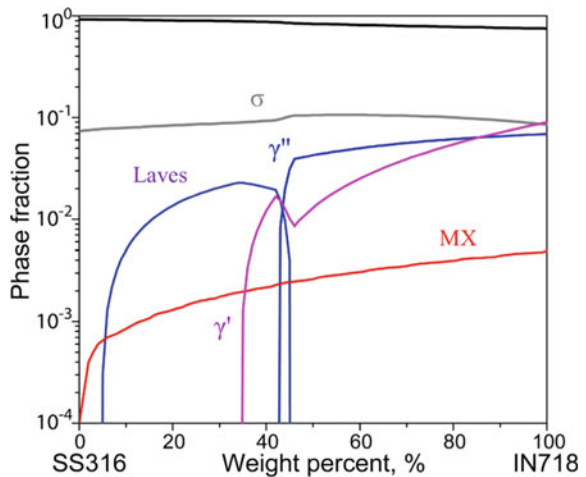
particles in the matrix (Fig. 3a2). They are only supposed to be the secondary phases of Laves and $M_{23}C_6$ [17, 18]. In the 25 wt.% IN718 component, Laves phase still forms along the grain boundaries, with an increase volume (Fig. 3b). Meanwhile, there are numerous needle-like secondary phase precipitated near the Laves phase, occupying the grain boundaries (Fig. 3b3). They are supposed to be the $NbNi_3$. The $NbNi_3$ phase is defined as δ phase in the TCNI8 database. Because δ phase is the stable phase and γ″ is the metastable phase in Ni-based superalloy, the δ phase is usually suspended in TCNI simulations to guarantee the formation of γ″ phase. That is why δ phase does not show in Fig. 4, replaced by γ′ and γ″ phase. When the weight percent of IN718 increases to 50 wt.%, the $NbNi_3$ phase is not found in the microstructure. Tremendous ultra-fine nanoprecipitates occur in the matrix, which is supposed to be γ′ and γ″ phases (Fig. 3c). According to the simulation result, γ′ and γ″ phases are formed replacing δ phase, with chemical formulas of $Ni_3(Ti, Al)$ and Ni_3Nb, respectively. It implies that the finer nanoprecipitates surrounding the Lave phase are γ″ phase and the relatively bigger ones away from the Laves phase are γ′ phase, which is also demonstrated in the following analyses for 75 wt.% and 100wt.% IN718 components (Fig. 3d4, e4). The TEM analysis of γ′ and γ″ phases in IN718 was studied in our previous work [19, 20]. As the increased content of IN718, γ′ and γ″ phases become separated from each other. The fraction of γ″ phase increases, which is well predicted in the simulations using TCNI8 database, as shown in Fig. 4. However, since Laves phase is a metastable phase, it is difficult to get a good prediction from thermodynamic simulation using the AM components with directly aging. Besides the analyzed phases above, MX secondary phase is always formed in the matrix as long as the matrix has the alloying elements, which has been confirmed in the SEM observations (Fig. 3a2–e2) and simulation result (Fig. 4).

As elucidated above, the gradient components with different compositions have remarkably different precipitation behaviors and transformations by the impact of the thermal aging treatment. This kind of precipitation transformations can be found in the gradient interface between 25 and 50 wt.% IN718, as presented in Fig. 3f. $NbNi_3$ or δ phase is reduced and partially transformed to γ′/γ″ phase. Another intriguing precipitation behavior is that the formation of γ″ is always near the Laves phase, and the formation of γ′ is far away from the Laves phase. Nonetheless, they are all nucleated and precipitated at grain boundaries. This is because the alloying elements like Nb, Ti, and Al at grain boundaries are high due to the segregation, which is suitable to form alloying element-rich γ′ and γ″ phases. Furthermore, during the isothermal aging heat treatment, the Laves phase gets dissolved gradually and releases the alloying elements, especially the element of Nb. Therefore, the Nb-rich γ″ phase is easy to form in the Nb-enriched area near the Laves phase. The Ti-rich γ′ phase is formed far away from the Laves phase because of the poverty of Nb. These nucleation and transformation between different phases are important and worth to exploit for the development of new FGMs using AM in the following work.

Conclusions

In the present work, the functionally graded material (FGM) from 316 stainless steel to Inconel 718 is fabricated using the powder-based LDED. The gradient microstructure and aging precipitation behaviors have been studied via experimental characterization and thermodynamic modeling. The FGM without cracks and distortions is successfully built using the LDED fabrication method. The composition of this FGM from 316 stainless steel to Inconel 718 is well controlled using hybrid powder feed system. The 75 wt.% IN718 component with fine and equiaxial grains is directly obtained from the laser deposition, which has a great potential for use in AM industry with the advantage of avoiding post-heat treatments. The aging precipitation behaviors in the FGM from Fe-based alloy to Ni-based alloy are for the first time studied. The phase transformations in these gradient components with different compositions are elucidated in depth. The diffusion and segregation of Ni, Nb, and Ti elements underly the transformation mechanism between Laves, δ, γ', and γ'' phases for the new development of FGMs using AM.

References

1. Mortensen A, Suresh S (1995) Functionally graded metals and metal-ceramic composites: Part 1 processing. Int Mater Rev 40:239–265
2. Liu Z, Meyers MA, Zhang Z, Ritchie RO (2017) Functional gradients and heterogeneities in biological materials: design principles, functions, and bioinspired applications. Prog Mater Sci 88:467–498
3. Hinojos A, Mireles J, Reichardt A, Frigola P, Hosemann P, Murr LE, Wicker RB (2016) Joining of Inconel 718 and 316 stainless steel using electron beam melting additive manufacturing technology. Mater Des 94:17–27
4. Yusuf SM, Gao N (2017) Influence of energy density on metallurgy and properties in metal additive manufacturing. Mater Sci Technol 33:1269–1289
5. Reichardt A, Dillon RP, Borgonia JP, Shapiro AA, McEnerney BW, Momose T, Hosemann P (2016) Development and characterization of Ti-6Al-4V to 304L stainless steel gradient components fabricated with laser deposition additive manufacturing. Mater Des 104:404–413
6. Sundman B, Jansson B, Andersson J-O (1985) The thermo-calc databank system. Calphad 9:153–190
7. Albrecht GF, Sutton SB, George EV, Sooy WR, Krupke WF (1998) Solid state heat capacity disk laser. Laser Part Beams 16:605–625
8. Künzel HM, Kiessl K (1996) Calculation of heat and moisture transfer in exposed building components. Int J Heat Mass Transf 40:159–167
9. Fann WS, Storz R, Tom HWK, Bokor J (1992) Direct measurement of nonequilibrium electron-energy distributions in subpicosecond laser-heated gold films. Phys Rev Lett 68:2834
10. Miracle DB, Senkov ON (2017) A critical review of high entropy alloys and related concepts. Acta Mater 122:448–511

11. Chen YY, Duval T, Hung UD, Yeh JW, Shih HC (2005) Microstructure and electrochemical properties of high entropy alloys-a comparison with type-304 stainless steel. Corros Sci 47:2257–2279
12. Sun R, Li L, Zhu Y, Guo W, Peng P, Cong B, Sun J, Che Z, Li B, Guo C (2018) Microstructure, residual stress and tensile properties control of wire-arc additive manufactured 2319 aluminum alloy with laser shock peening. J Alloys Compd 747:255–265
13. Winning M, Gottstein G, Shvindlerman LS (2001) Stress induced grain boundary motion. Acta Mater 49:211–219
14. Powell-Doğan CA, Heuer AH, Ready MJ, Merriam K (1991) Residual-stress-induced grain pullout in a 96% alumina. J Am Ceram Soc 74:646–649
15. Chaturvedi MC, Han Y (1983) Strengthening mechanisms in Inconel 718 superalloy. Met Sci 17:145–149
16. Slama C, Abdellaoui M (2000) Structural characterization of the aged Inconel 718. J Alloys Compd 306:277–284
17. Boes J, Röttger A, Becker L, Theisen W (2019) Processing of gas-nitrided AISI 316L steel powder by laser powder bed fusion—microstructure and properties. Addit Manuf 30:100836
18. Saboori A, Aversa A, Marchese G, Biamino S, Lombardi M, Fino P (2020) Microstructure and mechanical properties of AISI 316L produced by directed energy deposition-based additive manufacturing: a review. Appl Sci 10:3310
19. Zhao Y, Li K, Gargani M, Xiong W (2020) A comparative analysis of Inconel 718 made by additive manufacturing and suction casting: microstructure evolution in homogenization. Addit Manuf 36:101404
20. Zhao Y, Sargent N, Li K, Xiong W (2020) A new high-throughput method using additive manufacturing for materials design and processing optimization. Materialia 13:100835